https://doi.org/10.1016/j.jmst.2020.10.086

Atomic-Scale Dissecting the Formation Mechanism of Gradient Nanostructured Layer on Mg Alloy Processed by a Novel High-Speed Machining Technique

Hui Fu[a1], Xiaoye Zhou[c1], Bo Wu[a], Lei Qian[a] and Xu-Sheng Yang[a,b*]

[a]*State Key Laboratory of Ultra-precision Machining Technology, Advanced Manufacturing Technology Research Centre, Department of Industrial and Systems Engineering, The Hong Kong Polytechnic University, Hung Hom, Kowloon, Hong Kong, China (E-mail: xsyang@polyu.edu.hk)*

[b]*Hong Kong Polytechnic University Shenzhen Research Institute, Shenzhen, China*

[c]*Guangdong Province Key Laboratory of Durability for Marine Civil Engineering, School of Civil Engineering, Shenzhen University, Shenzhen, Guangdong 518060, PR China*

[1] These authors contributed equally to this work.

* Corresponding author. xsyang@polyu.edu.hk (X.-S Yang). Tel: +852-2766 6604

Abstract

Severe plastic deformation (SPD)-induced gradient nanostructured (GNS) metallic materials exhibit superior mechanical performance, especially the high strength and good ductility. In this study, a novel high-speed machining SPD technique, namely single point diamond turning (SPDT), is developed to produce effectively the GNS layer on the hexagonal close-packed (HCP) structural Mg alloy. The high-resolution transmission electron microscopy observations and atomistic molecular dynamics simulations are mainly performed to atomic-scale dissect the grain refinement process and corresponding plastic deformation mechanisms of the GNS layer. We find that the grain refinement process for the formation of GNS Mg alloy layer consists of elongated coarse grains, lamellar fine grains with deformation-induced-tension twins and contraction twins, ultrafine grains, and nanograins with grain size of ~ 70 nm along the direction from inner matrix to surface. Specifically, experiment results and atomistic simulations reveal that these deformation twins are formed by gliding twinning partial dislocations that are dissociated from the lattice dislocations piled up at grain boundaries. The corresponding deformation mechanisms are evidenced to transit from the deformation twinning to dislocation slip when the grain size is below 2.45 μm. Moreover, the Hall-Petch relationship plot and the surface equivalent stress along the gradient direction estimated by finite element analysis for the SPDT process are incorporated to quantitatively elucidate the transition of deformation mechanisms during the grain refinement process. Our findings have implications for the development of the facile SPD technique to construct high strength-ductility heterogeneous GNS metals, especially for the HCP metals.

Keywords: Gradient nanostructured Mg alloy; High-speed machining; Deformation twinning; High-resolution transition electron microscopy; Hall-Petch relationship

1 Introduction

It has been well-recognized that homogeneous nanograin (NG) metals (grain size lower than 100 nm) are very strong but extremely brittle (even those that are very ductile in their coarse-grain (CG) counterparts) [1]. In recent years, a new class of nanomaterials called gradient nanostructured (GNS) metals has received increasing attention due to its superb combination of strength and ductility. For example, GNS metals can be designed to a unique architecture with increasing gradually grain size from nanometer in the top surface to micrometer in the matrix core. Particularly, this special architecture can achieve the high strength-ductility synergy by combining the enhanced strength from the surface "hard" NG regions and the kept good ductility from the matrix core "soft" CG regions [2]. In addition to evading the strength-ductility trade-off dilemma, GNS metals may also exhibit the good wear resistance, low friction, enhanced fatigue resistance and excellent thermal stability [3-6], etc.

A variety of surface severe plastic deformation (SSPD) top-down approaches, such as surface mechanical grinding treatment [5], surface mechanical attrition treatment (SMAT) [3], high pressure torsion [7], rotationally accelerated shot peening [8], laser shock processing [9] and high-speed machining [10], etc., have been developing to produce the GNS by generating a gradient plastic strain field, which is extremely severe on the top surface layer and then gradually decreased towards the matrix region of metals. Note that conventional reducing-volume forming techniques, such as rolling, cutting and machining, are currently still widely applied to process billions of tons of materials for the metallic parts or products [11]. Therefore, high-speed machining SSPD technique can be developed flexibly as a simple and high-throughput surface-modifying manufacturing method to effectively machine the bulk materials into the desired shapes with GNS layers, thereby leading to the additional high-performance mechanical properties, especially the high strength-ductility synergy [10]. For example, a well-established hard turning method has been used to machine steels with hard surface in the bearing steel industry [12].

The plastic deformation mechanisms contributing to the grain refinement process of SSPD-induced GNS metals have been extensively investigated, especially for the metals with cubic crystal structures. For instance, the GNS refinement process of face-centered cubic (FCC)

metals are mainly resulted from two types of dislocations activities (i.e., perfect dislocations and partial dislocations) that are competitively happened on {111} crystallographic planes [13]. According to the nature of metals (e.g., stacking fault energy, grain size and composition, etc.) and the status of gradient stress/strain received form the SSPD process, these two competitive dislocations activities can lead to the various refinement mechanisms, including the activities of dislocation subdivision [14], deformation twin fragmentation [15], twin-twin intersections [16] and phase transformation [17, 18], etc.

However, much fewer studies have been devoted to the refinement mechanisms of hexagonal close-packed (HCP) GNS metals fabricated by SSPD techniques, especially by high-speed machining. Compared with metals with cubic structures, HCP structural metals possess lower crystallographic symmetry and fewer independent slip systems. The primary slip system in HCP crystal is the basal <a> slip on its densest {0001} basal plane, which can only provide two independent slip systems and falls far short of five independent slip systems required for arbitrary shape change in polycrystals. As a consequence, other non-basal planes slip along either <a> or <a+c> directions, as well as twins are needed to be activated to improve the plasticity of HCP metals [19]. However, the activations of dislocation slip and deformation twinning systems in HCP alloys are quite different size-dependent compared with cubic alloys. In contrast, on one hand, CG layers in HCP metals usually need twinning to accommodate plastic deformation in addition to dislocation slip, because there are not five independent deformation systems, as required by the von Mises criterion for compatibility. One the other hand, deformation twinning becomes more difficult with decreasing grain size along the gradient direction and rarely observed below a critical grain size in HCP NG layers. These diverse deformation modes are responsible for the complex refinement mechanisms in the HCP GNS metals [20-22]. For example, Sun et al. [20] studied the grain refinement process of GNS AZ91D alloy produced by SMAT technique. It could be divided into three steps: the cutting of original CGs by twinning platelets, the arrangement of dislocations along subgrain boundary, and the formation of NGs caused by dynamic recrystallization (DRX) of dislocation. Shi et al. [21] also found that CGs are refined to subgrains by the combination of twins and dislocations in SMAT-induced GNS Mg-3Gd alloys, in which dislocation slips and stacking faults (SFs) were revealed to impel the subgrains to NGs by lattice rotating through dislocation arrays

slipping. More recently, Chen et al. [22] found that the formation of gradient grain size in SMAT-induced Mg-Al-Zn alloys is attributed to the twins and dislocation slips. However, it is worth noting that the twins are activated through the whole GNS layer based on microstructure observations. The above description indicates that the grain refinement process and corresponding grain size-dependent plastic deformation mechanisms of the SSPD-induced GNS layer on HCP metals are still unclear. Consequently, the detailed examinations are highly demanded to uncover the microstructural evolution along the gradient direction of the SSPD-induced GNS layer on HCP metals, especially the atomic nucleation and growth mechanisms of different deformation twins induced by gradient strain-rate deformation.

In this study, a novel high-speed machining SPD technique, namely single point diamond turning (SPDT), is developed to produce effectively the GNS layer on the HCP Mg-4wt.%Li (L4) alloy. The SPDT technique can achieve large strains (typically 2-10) and high strain rates (up to 10^6 s^{-1}) on the specimen with many unique advantages, such as short process time, no heating required, cost effectiveness, good controllability, and excellent surface finish [23]. In addition, addition of lithium in Mg not only offers a great potential to enhance the deformation capacity of the material, but also because it allows to substantially lower the density of the already light Mg even more [24]. Grain refinement process and corresponding grain size-dependent plastic deformation mechanisms of the SPDT-induced GNS layer (NGs with grain size of 70 nm in the top surface) are dissected at the atomic-level by high-resolution transmission electron microscopy (HRTEM) observations, atomistic molecular dynamics (MD) simulations as well as finite element analysis (FEA). Particularly, the atomic mechanisms of two types of deformation twins, i.e., tension twins (TTWs) and contraction twins (CTWs), involved in the refinement process are revealed by HRTEM and atomistic simulations. Besides, we confirm the transition of the deformation twinning in fine grains (FGs) to the dislocation slip in ultrafine grains (UFGs) and NGs when the grain size is below 2.45 μm. Moreover, the Hall-Petch relationship plot and the surface equivalent stress estimated by FEA from the SPDT process are incorporated to quantitatively understand this transition of deformation mechanisms. Rather than the exterior machining parameters, this study provide a deep dissecting of the relationship between microstructure evolution and corresponding deformation modes for the fundamental understanding of formation mechanism of GNS layer during SPDT

processing.

2 Methods

2.1 GNS layer produced by SPDT

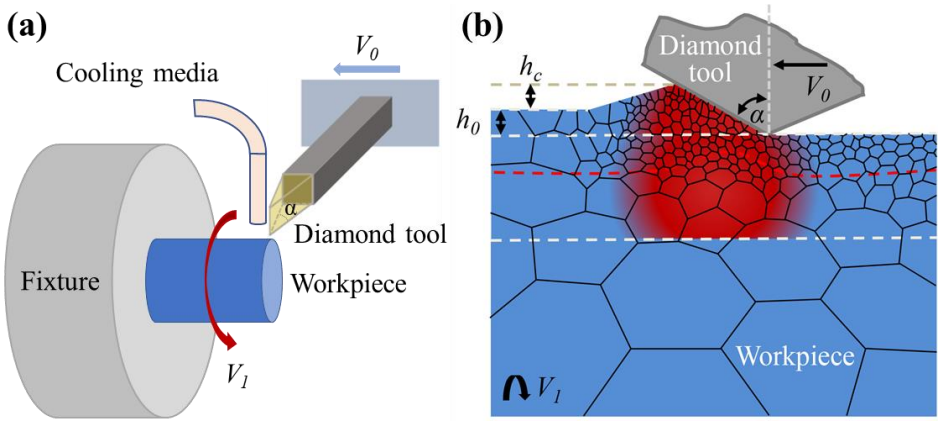

Fig. 1 Schematic diagrams (a) the SPDT process and (b) the SPDT-induced surface prow deformation for the formation of GNS, respectively.

The CG L4 alloy was received as an extruded bar with grain size of ~ 21 μm after annealed at 200 ºC for 1 h for the homogenization. The cylindrical workpiece with 10 mm in diameter and 15 mm in length was cut from the annealed sample for the SPDT process, which was conducted in Moore Nanotech 450UPL SPDT machine (Moore precision tools Inc. USA), as the configuration schematically shown in Fig. 1(a). The sample can be turned at extremely high spindle speed (V_1) with certain tool rake angle (α), cutting depth (h_0), cooling and lubricating medium (e.g., oil and liquid nitrogen). Notably, when the tool rake angle α is modified as highly negative in the SPDT process, this high-speed machining process would lead to a pileup of material (prow) ahead of the tool, as schematically shown in Fig. 1(b), which "compress" back into the surface and thus result in the SSPD process rather than the only removal of material. In this connection, the refinement principle of SPDT developed in this work is similar to some other conventional SSPD techniques [5]. Accordingly, 20 passes of SPDT high-speed machining process, with the V_1 of 500 rpm, h_0 of 10 μm, α of 30º and feed rate (V_0) of 5 mm/min, are applied to cause and accumulate the SSPD process for the generation of GNS layer on the sample. These SPDT parameters in the present work will induce the approximately equivalent strain and strain rate on the specimen in comparison with some conventional SSPD techniques.

2.2 Mechanical properties and Microstructure characterizations

Mechanical properties are the embodiment of a material's microstructure. In our work, the variation of the hardness of the SPDT L4 sample along the depth direction from the surface to the matrix was determined to verify the success of the GNS formation. The nanoindentation experiments of the SPDT L4 sample were conducted at room temperature using a Hysitron TI-900 Triboindentor with a Berkovich diamond indenter. The polished specimens at different depth layers of the SPDT sample were loaded to a max load of 5 mN with a loading rate of 0.25 mN/s, and then unloaded with the same rate after holding the max load for 5 s. The nanoindentation experiment at each depth layer was repeated at least 9 times for the meaningful data statistics.

The overall cross-sectional microstructures of the original and SPDTed L4 specimens were observed by a Leica DMLM optical microscopy (OM) to verify the occurrence of the GNS layer. To further analyze the microstructure of matrix and GNS layer, electron backscatter diffraction (EBSD) map was obtained by TESCAM MIRA3. X-ray diffraction (XRD) was performed at different depth layers of the SPDTed specimens by the Rigaku SmartLab 9kW-Advance diffractometer with Cu Ka radiation at a scan from 30° to 60° with a step of 0.02 and a permanence time of 2s. Moreover, the HRTEM plane-view observations were performed using a field emission JEM-2100F operated at voltage of 200 kV. According to the OM observations and the variation of hardness along the depth direction in the nanoindentation tests, TEM slices were taken from different depth layers of the SPDTed specimens to atomic-scale study the sequential evolutions of the microstructure and grain size. TEM slices were mechanically polished to ~25 μm from the side away from the observation layer. After that, the TEM foils were glued to the copper ring for the further single side ion milling on the precision ion polishing system Gatan 691. For the TEM observation at a certain depth layer, we first mechanically polished the specimen from the topmost surface side to this depth layer. Then, this specimen was mechanically polished from another side away from the observation layer, forming a ~ 25 μm-thick TEM slice. The single-side ion milling mode was subsequently conducted to thinning the TEM slice from another side away from the observation layer. After that, the TEM observations were performed on this depth layer from the topmost surface-side

direction. Therefore, the damage of the target depth layer during the ion milling process can be avoided for the TEM observations. In addition, liquid nitrogen was used during ion milling to obtain cleaner and less damaged TEM samples.

3 Simulations

3.1 Molecular dynamics simulations

Atomistic MD simulations were conducted using the LAMMPS software to assist the understanding of the microstructure evolution during SPDT process. Polycrystalline model was built using 2-D Voronoi tessellation to separate cubic cells into 9 polyhedrons. Each polyhedron was filled with HCP Mg atoms aligned along a random orientation. The as-built model has an average in-plane grain size of 24 nm, while the out-of-plane dimension is 10 nm. Periodic boundary conditions were imposed along all directions. The Mg-Li interatomic interaction was described by an Embedded Atom Method potential [25]. After the constructions of the polycrystalline model, the annealing process of system was first heated to 700 K for 1 ns and then cooled down to 300 K in 0.3 ns to obtain the equilibrium structure. The turning tool was modeled as a rigid body diamond quadrangular with the same out-of-plane dimension as the model. Before the leftward turning, the turning tool was placed on the top surface and lowered down to a cutting depth of 10 nm in the model, with a rake angle α of 30 degree. The tool was then moved leftwards with the cutting speed of 500 m/s. When one pass had been finished, the tool was again lowered down to the same depth followed by a new round of turning. The simulated turning process was repeated 10 passes.

3.2 Finite element analysis

Given the limitations in scale (10 nm cut) and velocity (500 m/s speed) in MD simulations with smaller system, the stress distribution along the depth direction of the GNS layer will be obviously larger than that in real experiments. Therefore, a commercial FEA software ABAQUS was performed to construct the comparable system and estimate the equivalent stress distribution along the depth direction of L4 alloy in the SPDT process. Specifically, the empirical Johnson-Cook constitutive model is used to express the stress-strain/strain rate relationship of L4 alloy during the SPDT process, which can be expressed as follows [26]:

$$\sigma = [A + B\varepsilon^{n}]\left[1 + C\ln\left(\frac{\dot{\varepsilon}}{\dot{\varepsilon}_0}\right)\right] \quad (1)$$

where σ is the equivalent flow stress, ε is the equivalent effective strain, $\dot{\varepsilon}$ is the plastic strain rate, and $\dot{\varepsilon}_0$ is the reference strain rate ($\dot{\varepsilon}_0$=1 s^{-1}), respectively. In Eq. (1), coefficient A is the yield strength, B is the hardening modulus, C is the strain-rate sensitivity coefficient, and n is the hardening coefficient. The Johnson-Cook constitutive model has been widely employing in FEA to estimate the equivalent stress distribution during the metal cutting, which is highly influenced by the geometry of cutting tools and cutting parameters . In our FE simulations, the diamond tool was considered to be a rigid -body and the cutting direction is along the circumferential direction of the workpiece. As the L4 alloy is a single-phase α-Mg solid solution alloy, the detailed Johnson-Cook constants values of A, B, C and n for α-Mg alloy are based on previous study. [27]. The rake angle of diamond tool (30°), the cutting velocity (262 mm/s) and the depth of cut (10 μm) in FE simulations were assigned as the same as that in the experimental process, which ensures the simulated results can be in good agreement with the experiments.

4 Results

4.1. Microstructure evolution of GNS layer by SPDT process

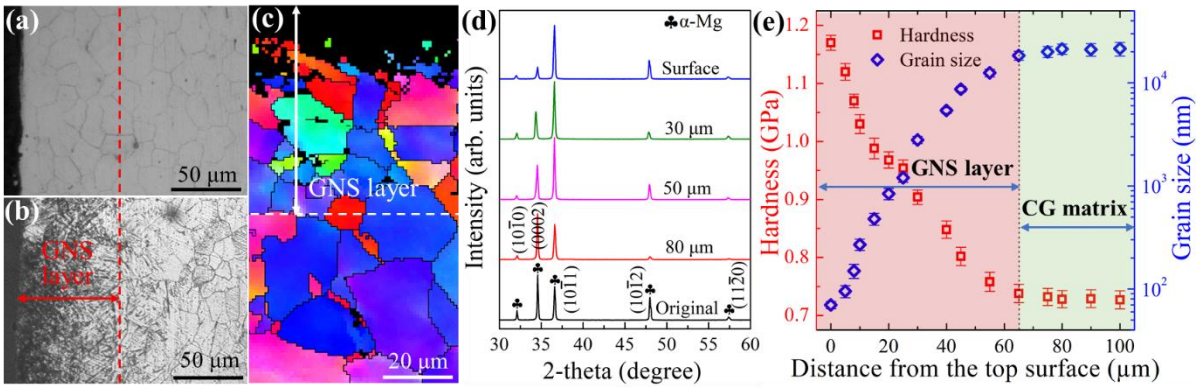

Fig. 2 Cross-sectional OM images of the (a) original and (b) SPDT L4 alloy. (c) EBSD map of the cross-sectional surface of SPDT L4 alloy. (d) XRD patterns of original and SPDT alloy at different depths of 80 μm, 50 μm, 30 μm, and surface, respectively. (e) Variation of both hardness and grain size against the distance from the topmost surface to the CG matrix of the SPDT L4 alloy.

Fig. 2(a)-(b) show the cross-sectional microstructure of original and SPDT L4 samples, respectively. The original L4 alloy exhibits homogeneous equiaxed grains with average grain

size of 21 μm. However, about 65 μm-thick GNS layer with continuously increasing grain sizes from nanoscale in surface layer to microscale in core region is formed in the SPDT sample, as shown in Fig. 2(b), which is attributed to the gradient distributions of SPDT-induced stresses and strain rates. The microstructure of the cross-section is further investigated using EBSD as shown in Fig. 2(c). The top layer regions could not be indexed and appear dark in the EBSD maps, a likely result of the small grain sizes with high residual strain induced by the SPD process, similar to the referenced study [28]. The XRD patterns of original and SPDT samples taken in different depth layers from surface are illustrated in Fig. 2(d). The XRD pattern of 80 μm depth layer in SPDT sample is similar to that of the original sample with a single α-Mg phase. It indicates that 80 μm depth region still belongs to undeformed area. Compared with the undeformed matrix, peaks of XRD patterns in several representative GNS layers (50 μm, 30 μm depth and surface) are clearly broadened. It indicates that grain refinement and introduction of lattice microstrains occur in these GNS layers. Strain-induced texture transformation is also a key deformation phenomenon in the HCP Mg alloys. It can be found that the matrix has a weak (0002) basal texture because of the homogeneous annealing treatment of the received L4 extrusion bar. However, the intensity of $(10\bar{1}1)$ plane is higher than the intensity of (0002) plane in all GNS layers. It indicates there is a nearly random grain orientation in the GNS layer, without obvious texture structure. Fig. 2(e) gives the variation of hardness along the depth direction from the topmost surface to the matrix of the SPDT L4 sample, together with the corresponding average grain size statistically determined based on the TEM characterizations in the following sections. The hardness (average grain size) at the topmost surface layer is ~1.17 GPa (70 nm), which is gradually decreased (increased) along the depth direction to be ~ 0.73 GPa (21 μm) in the ~ 65 μm depth layer and then unchanged onwards, suggesting that a GNS layer with a thickness of ~ 65 μm is successfully created in the SPDT L4 sample. This result is consistent with our OM observations. In the following sections, the formation mechanisms of GNS layer will be elaborated by HRTEM characterizations and atomistic MD simulations.

4.1.1 TEM characterizations for the overall grain refinement process

Overall microstructural evolution for formation of GNS layer in the SPDT samples by

TEM observations are shown in Fig. 3. Fig. 3(a) shows the bright-field (BF) TEM image of the region that is about 65 μm below the top surface, near to the undeformed matrix region. The CGs are obviously elongated in this deformed layer. The width of elongated grain is reduced to several microns. Combined with the OM results, this layer can be recognized as the transition region between the GNS layer and the undeformed matrix. Dense dislocations (marked by white triangle) are emitted from the grain boundaries (GBs). The inset in Fig. 3(a) shows the atomic structure of GBs, where the dense basal dislocations are emitted, reveling that the deformation stress in this transition layer is gentle. Fig. 3(b) is the BF TEM image of the layer about 50 μm below the top surface. With increasing stress and strain rate, the elongated CGs are further refined to lamellar FGs with the width of ~ 2 μm. In addition, profuse lenticular twins originated from GB with hundred nanometers thickness are also observed in this layer, as evidenced by the corresponding selected area electron diffraction (SAED). The SAED pattern (Fig. 3(c)) confirms the deformation twin shown in Fig. 3b is the $\{10\bar{1}2\}$ TTW, which rotates the crystal 86° along $<\bar{1}2\bar{1}0>$ axis. It suggests that the dominated deformation mechanism for the grain refinement in this layer is transited from dislocation slip to deformation twinning. When the layer depth comes to ~30 μm below the top surface, it is found that the width of lamellar FGs is continually reduced to be lower than 1 μm and the TTW is hardly observed. Alternatively, another type of dense needle-like twins with the thickness of tens nanometers are observed in this layer as indicated in Fig. 3(c). It can be seen that these twins are also originated from GB, similar to the TTWs. Corresponding SAED pattern is parallel to $[1\bar{2}1\bar{3}]$ zone axis, indexing that the diffraction patterns of the matrix and twin are mirror reflections across the $(1\bar{1}01)$ plane, well consistent with the typical $\{10\bar{1}1\}$ CTW. Therefore, it suggests that the dominated deformation mechanism for the refinement in this depth layer is still the deformation twinning but changed to the case of CTW, which has not been reported in the previous literature regarding the SSPD-induced GNS layer on HCP metals. TEM examination of the layer about 15 μm below the surface shows the scattered areas of residual lamellae and some new polygonal UFGs with hundreds of nanometers in size as indicated in Fig. 3(d). Randomly oriented NGs with average grain size of ~95 nm are generated

in the layer about 5 μm below the surface, as evidenced by the TEM image and associated continuous diffraction rings in the inserted SAED pattern in Fig. 3(e). Finally, Fig. 3(f) gives the TEM image for the microstructure in the topmost surface layer of the SPDT L4 alloy, demonstrating the equiaxed NGs with the smallest grain size. As shown in upper right inset, the grain size varies from 40 nm to 100 nm, denoting the average grain size of 70 nm. It can be clearly seen that lots of line-like structures (red arrows) exist in these NGs rather than a "clean" grain mentioned in previous work [20] of SMAT Mg alloy. It can be inferred that the refinement of NGs is caused by rotation DRX. To sum up, the grain refinement mechanisms for the formation of the GNS layer in SPDT L4 alloy consists of elongated CGs, lamellar FGs, TTWs, DTWs, UFGs and NGs along the direction from inner matrix to surface. Further atomic-level characterizations of microstructure evolution by HRTEM are shown in following section.

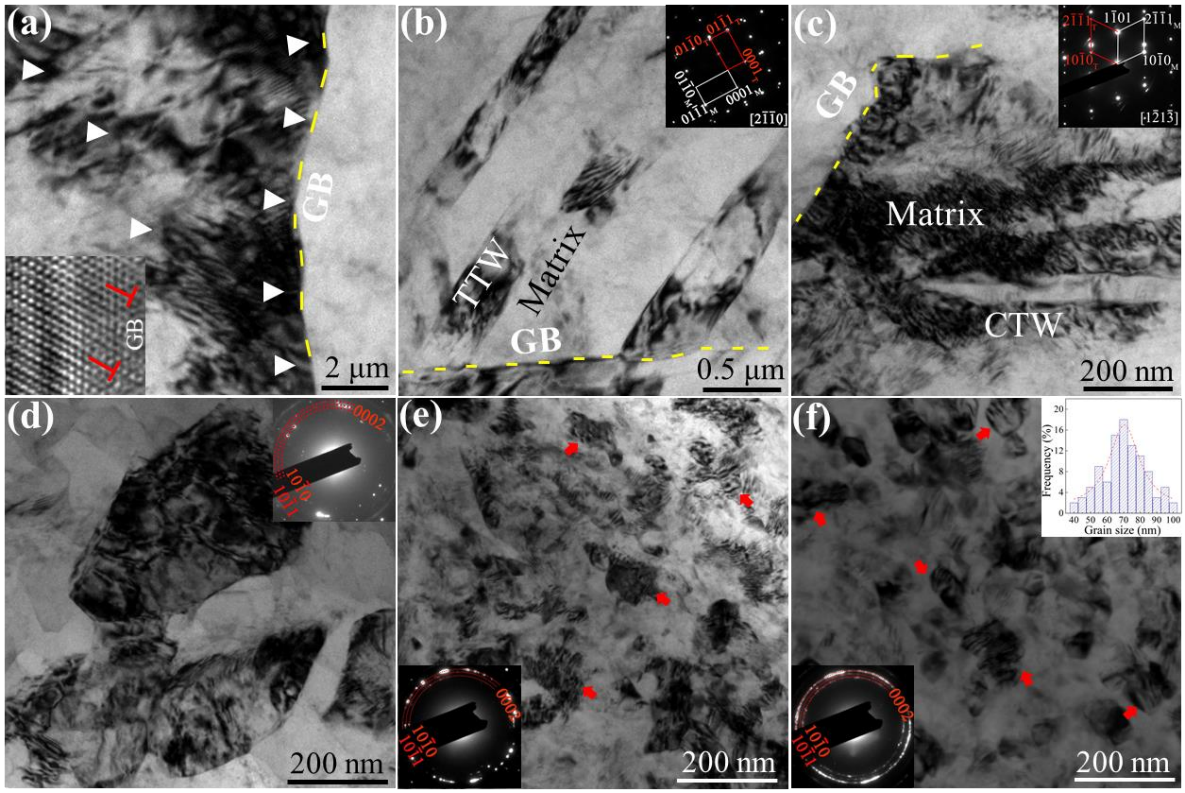

Fig. 3 Typical longitudinal section BF TEM images of the SPDT L4 alloy at different depths. (a) 65 μm. (b) 50 μm. (c) 30 μm. (d) 15 μm. (e) 5 μm. (f) Topmost surface. Insets are the corresponding HRTEM image, SAED patterns and grain size distribution.

4.1.2 HRTEM characterizations for two deformation twins

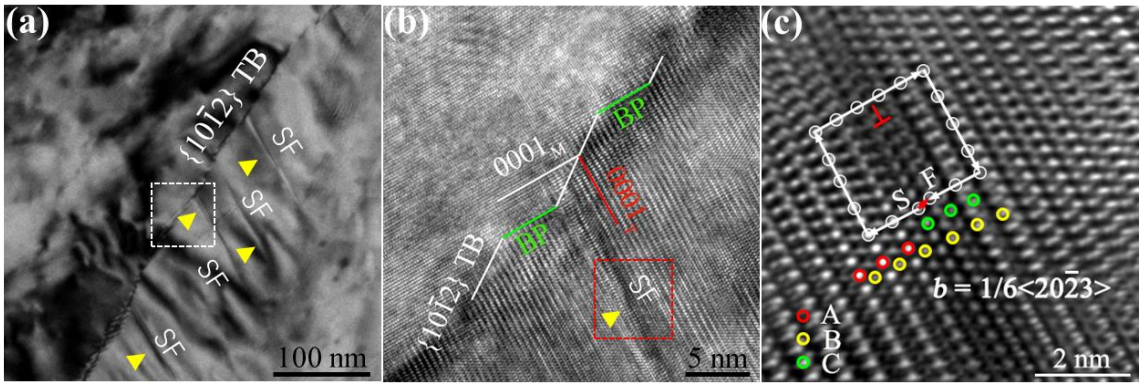

Fig. 4 (a) TEM image of the TTW. (b) HRTEM of TB of dotted square in (a). (c) Fourier-filtered image of SF.

Fig. 4(a) is the enlarged TEM image of the TTW. It can be seen that the twinning boundary (TB) is serrated, with the emission of lots of SFs (grey stripes partly indicated in yellow triangles). Fig. 4(b) is the HRTEM image of TB marked by the white dashed square in Fig. 4(a). It shows that the TTW TB consists of coherent $\{10\bar{1}2\}$ TB (denoted by solid white lines) and steps (marked by solid green lines) along specific plane. The steps correspond to the Basal-Prismatic (BP) interfaces, which place basal and prismatic planes face to face, namely $\{0001\}//\{10\bar{1}0\}$ interfaces. The BPs boundaries are associated with pile-up and rearrangement of twinning dislocations or disconnections (TDs) according to previous studies [29]. Moreover, one typical SF stopped in the TB is characterized at the atomic level by inverse fast Fourier transformation (IFFT) image as shown in Fig. 4(c), where the Burgers vectors are constructed with Letters S and F respectively denoting the start and finish of the Burgers circuits. The closed-packed {0002} planes of the perfect HCP crystals possess an …ABABAB… stacking sequence. The closure failure of the Burgers circuit indicates that a $1/6<20\bar{2}3>$ Frank partial dislocation alter this stacking sequence to be … ABABABCBCBCB …. As this process evolves the insertion of a basal plane, this SF is an interstitial-type I_1 fault [30], denoting the dislocation reaction as follow:

$$\frac{1}{2}<0001>+\frac{1}{3}<10\bar{1}0>\rightarrow\frac{1}{6}<20\bar{2}3> \quad (2)$$

This result is consistent with the semi-coherent BP boundary caused by TDs [31]. It also indicates the non-basal slips are activated to refine the grains in this layer.

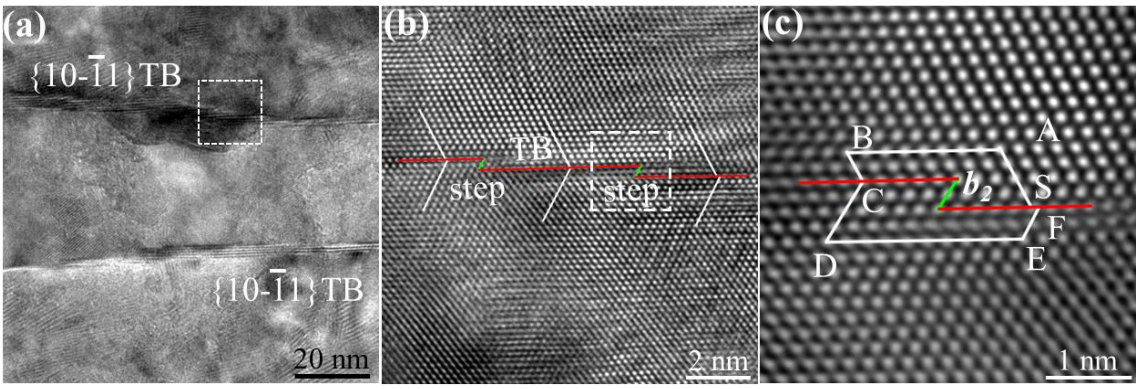

Fig. 5 (a) TEM image of the CTW. (b) HRTEM of TB of dotted square in (a). (c) Fourier-filtered image of step.

In addition, Fig. 5(a) is the enlarged TEM image of the CTW. A typical slender shaped twin with a width of ~50 nm is observed and the TBs of CTW are also serrated. There are a lot of steps in the TBs as shown in the HRTEM image (Fig. 5(b)) taken from the white dashed square in Fig. 5(a). The steps are related to the TDs in CTW. To confirm the type of TDs, a Fourier-filtered image (Fig. 5(c)) of step is taken from the white dashed square in Fig. 5(a). As shown in Fig. 5(c), a two atomic-layer step ($\boldsymbol{b_2}$) is observed in the $\{10\bar{1}1\}$ TB of CTW. Since the traditional Burgers circuit cannot be applied to calculate the atomic disarrangement at interfacial defects, herein a circuit mapping method is used to draw Burgers circuit around the steps on TB and further to quantify the Burgers vector of TDs by the method of Pond [32]. Fig. 5(c) gives a closed circuit SABCDEF that is constructed around $\boldsymbol{b_2}$. The translation $\boldsymbol{SC}$ represents the total mapped circuit element in the twin crystal and is designated as $\boldsymbol{t(\lambda)}$. Similarly, the total mapped element $\boldsymbol{CF}$ in the matrix crystal is designated as $\boldsymbol{t(\mu)}$. Thus the total mapped circuit SF when expressed in the coordinate system of the upper crystal is given by $\boldsymbol{t(\lambda)+Pt(\mu)}$, where $\boldsymbol{P}$ is the transformation matrix [32]. Adopting the Right-Hand convention and taking the line direction of the defect to be out of the page, $\boldsymbol{b_2}$ is equal to FS and therefore given by

$$\boldsymbol{b_2} = \boldsymbol{FS} = -(\boldsymbol{SC} + \boldsymbol{CF}) = -[\boldsymbol{t(\lambda)} + \boldsymbol{Pt(\mu)}] = \frac{4\kappa^2-9}{2(4\kappa^2+3)}[\bar{1}01\bar{2}] + \frac{1}{6}[\bar{1}2\bar{1}0] \quad (3)$$

where κ is the lattice parameters ratio c/a. This result is consistant with previous studies [33].

4.1.3 HRTEM characterizations for UFGs and NGs

Fig. 6(a) is the enlarged TEM image of UFG with the grain size ~400 nm. Fig. 6(b) shows

a lot of straight and thin SFs exist in the grain interiors. The presence of streaking along the <0001> directions in corresponding FFT pattern in the inset of Fig. 6(b) testifies that the faults are (0001) basal-plane SFs. It means that basal-plane SFs become the primary crystalline defects in this deformed layer. Note that the formation of the SFs is always related to the dislocation gliding. IFFT images in Fig. 6(c) and Fig. 6(d) are used to determine the types of SFs and their bounding dislocations. The Burgers vectors ***b*** of the partial dislocations forming I_1 and I_2 SFs are determined by the Burgers circuits drawing in (c) and (d), respectively. The closure failure of the Burgers circuit in Fig. 6(c) indicates that it is a $1/6<20\bar{2}3>$ Frank partial dislocation. The stacking sequence shows that this partial dislocation induces an I_1 SF. However, an I_2 stacking sequence …ABABABCACACA… formed by a 30° $1/3<10\bar{1}0>$ Shockley partial dislocation can be identified in Fig. 6(d). Based on above analyses such as this, intrinsic I_1 and I_2 SFs are the most frequently observed in the UFGs. Fig. 6(e) is the enlarged TEM image of one typical NG with the grain size ~75 nm. Similar to UFGs, there exist slather SFs in the NG interior. The enlarged SFs in this grain are indicated by a pair of red arrows in the HRTEM image of Fig. 6(f) (showing the rectangular area marked in Fig. 6(e)). These I_1 and I_2 SFs nucleate at the GBs and grow into the grain interior via partial dislocation emission from the GBs. Simultaneously, the formation of SFs involved the partial dislocation are believed to have a significant effect on deformation behavior especially at the nanometer scale. The existence of dislocation arrays including basal dislocations, prismatic dislocations and pyramidal dislocations should be the evidence of rotation DRX. These dislocations will lead to the formation of the low angle GBs and the lattice rotation when dislocation arrays inside the grain slip to the boundaries. It could be expected that dislocation arrays at different planes will result in different rotating directions of the lattice in subgrains. In addition, dislocations accumulate or annihilate in the boundaries by gliding through the grain interior to accommodate the plastic strain, which is a process of internal energy decrease. Therefore, the misorientation between two subgrains gradually increases through dislocation slips and eventually the low angle boundary becomes into a high angle GB with randomly orientations, as the SAED of NGs in the topmost layer shown in Fig. 3(f). The extremely high strain rate at room temperature like what is carried out in the present work may affect the operation of non-

basal slip system. It reveals the refinement mechanism in NGs is rotation DRX which caused by dislocation slips.

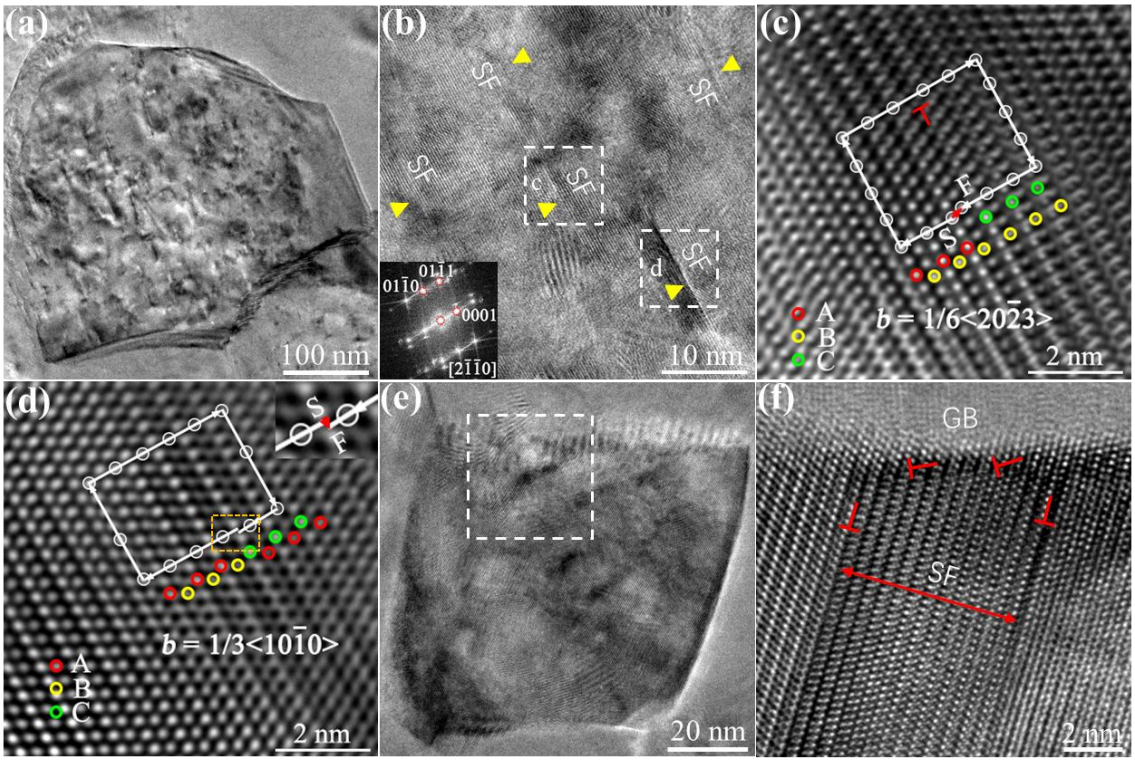

Fig. 6 (a) TEM image of UFG. (b) HRTEM image of UFG, inset is the FFT pattern. (c), (d) Fourier-filtered image of SF marked by white dashed square in (a). (e) TEM image of NG. (f) HRTEM image of SF from the marked region in (e) and high density of dislocations exists in the GBs.

4.2 Simulations

4.2.1 Atomistic MD simulations of the SPDT process

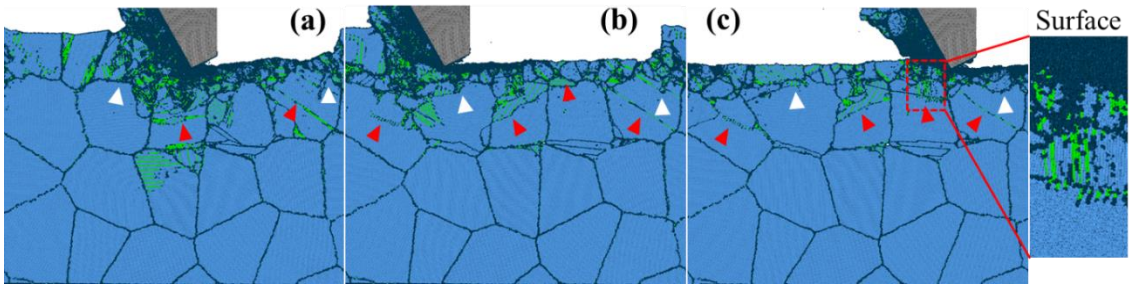

Fig. 7 (a-c) Microstructure evolution of the MD simulation model at three different stages during cutting, from (a) stage 1, (b) intermediate stage 2, to (c) stage 3. Inset is the enlarged image of red dash region in (c). The atoms are colored using common neighbor analysis.

Fig. 7(a-c) respectively give the representative three different stages of typical simulated cutting processing to dissect the plastic deformation mechanisms for the refinement process of GNS along the gradient direction. Note that plastic deformation mechanisms for the refinement

process is well consistent with the SPDT experiment results. As shown in the inset from Fig. 7(c), the topmost surface suffers the most SPD during the simulated SPDT process, generating the densest dislocations and SFs nucleated from the GBs, which pass through the interior of grains for the refinement. In addition, the strain and strain rate caused by the simulated SPDT process are also gradually diminished from the treated top surface to the inner matrix. Accordingly, the refinement effects of the grains beneath the top surface are gradually reduced, thus generating the GNS layer on the Mg alloy. Particularly, Fig. 7(a-c) shows that profuse TTWs (red arrows) and CTWs (white arrows) are also found to be triggered in the simulated SPDT process from the GBs in the deformed grains in the subsurface layer. The TTWs are found to be nucleated with higher density in the deeper layer if in comparison with CTWs. This result is consistent with the TEM observations.

4.2.2 Equivalent stress calculated by FEA in SPDT processing

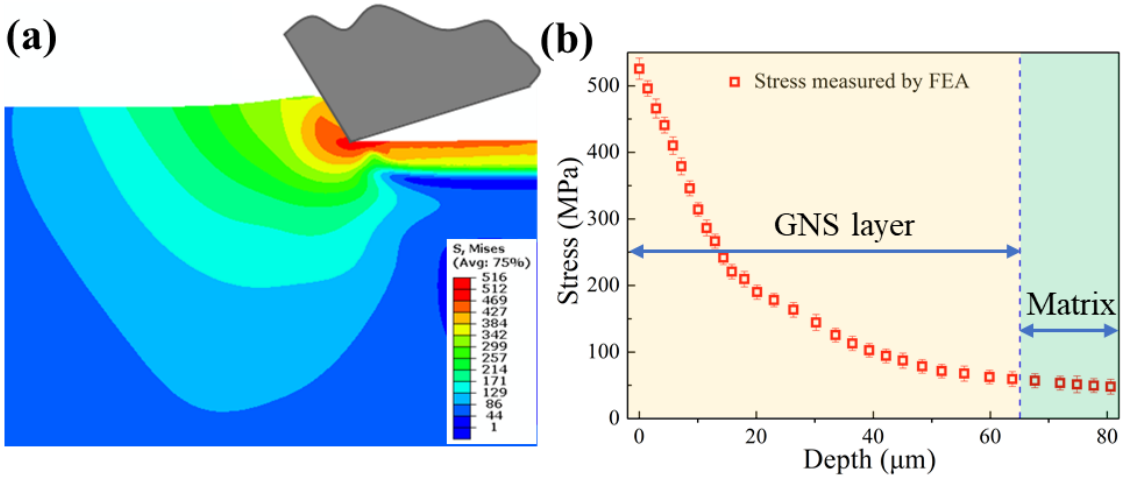

Fig. 8 (a) Contour map distributions of equivalent stress in SPDT sample. (b) The statistics of varied equivalent stress with depth calculated by FEA in SPDT processing.

In the SPDT process, measurement of the undeformed (h_0) and deformed chip thicknesses (h_c) provide an estimate of shear strain (γ) in the workpiece surface [34]:

$$\gamma = \frac{\lambda}{\cos\alpha} + \frac{1}{\lambda\cos\alpha} - 2\tan\alpha \tag{4}$$

where λ is the chip thickness ratio (h_c/h_0), which is about 0.5 according to the SPDT process parameters in this work. α is tool rake angle, which is 30° in the SPDT process. The effective strain can be given by $\varepsilon = \left(1/\sqrt{3}\right)\gamma$ [35], thus the effective strain ε in the workpiece surface is about 0.89. Under the localized deformation conditions, the plastic strain rate $\dot{\varepsilon}$ is well

approximated as [34]:

$$\dot{\varepsilon} = \frac{d\varepsilon}{dt} = \frac{\varepsilon V}{\Delta} \tag{5}$$

where Δ is the thickness of deformation zone, about 65 μm based on the microstructure observation and hardness measurement. V is the deformation rate, equal to the linear velocity (262 mm/s) of workpiece rotation. The strain rate is about 3.6×10^3 s^{-1} calculated by Eq. (5). Therefore, the equivalent stress in the surface of sample in the SPDT process is about 535 MPa, according to the Johnson-Cook model in Eq (1). Furthermore, this Johnson-Cook model is used in FEA simulations to calculate the equivalent stress distribution along the depth direction during the SPDT process, as shown in Fig. 8. Combined with the contour map and statistics equivalent stress distribution plot, it can be seen that equivalent stress exerted in the workpiece is gradually reduced. The equivalent stress profile can be divided into two zones. Starting from the surface to ~65 μm depth, the stress decreases rapidly with the depth. It is followed by a relatively constant stress when the depth is deeper than 65 μm. The strain and strain gradient are also small in the second zone. It can be inferred that affected cutting depth is ~65 μm. This simulation results are consistent with our experiment observations. Consequently, the experimental and simulation results reveal that deformation mechanisms for the refinement process of GNS layer on Mg alloys are grain size-, and stress/strain rate-dependent.

5 Discussion

From the above results of HRTEM characterizations and atomistic MD simulations, we have revealed the grain refinement process and corresponding plastic deformation modes along the depth direction of the GNS layer on HCP L4 alloy produced by developing a novel SPDT high-speed machining. More specifically, (i), The microstructures of the GNS layer on SPDT L4 alloy are gradually changed from elongated CGs, lamellar FGs by TTWs and CTWs, UFGs, to NGs from inner matrix to topmost surface, where the CTWs are for the first time characterized in the SSPD-induced GNS HCP metals. (ii) The corresponding dominated deformation mechanisms are transited from dislocation slip to deformation twinning when the elongated CGs are refined to FGs. When the FGs are continually refined to UFGs and NGs, dislocation slip becomes the dominated deformation mode again. Two critical issues, i.e., (i)

the atomic movement mechanisms for the nucleation and growth of TTW and CTW, and (ii) the quantitatively understanding of grain size-dependent competition deformation mechanisms between deformation twining and dislocation slip, will be elaborated in this section.

5.1 Nucleation and growth mechanisms of deformation twinning

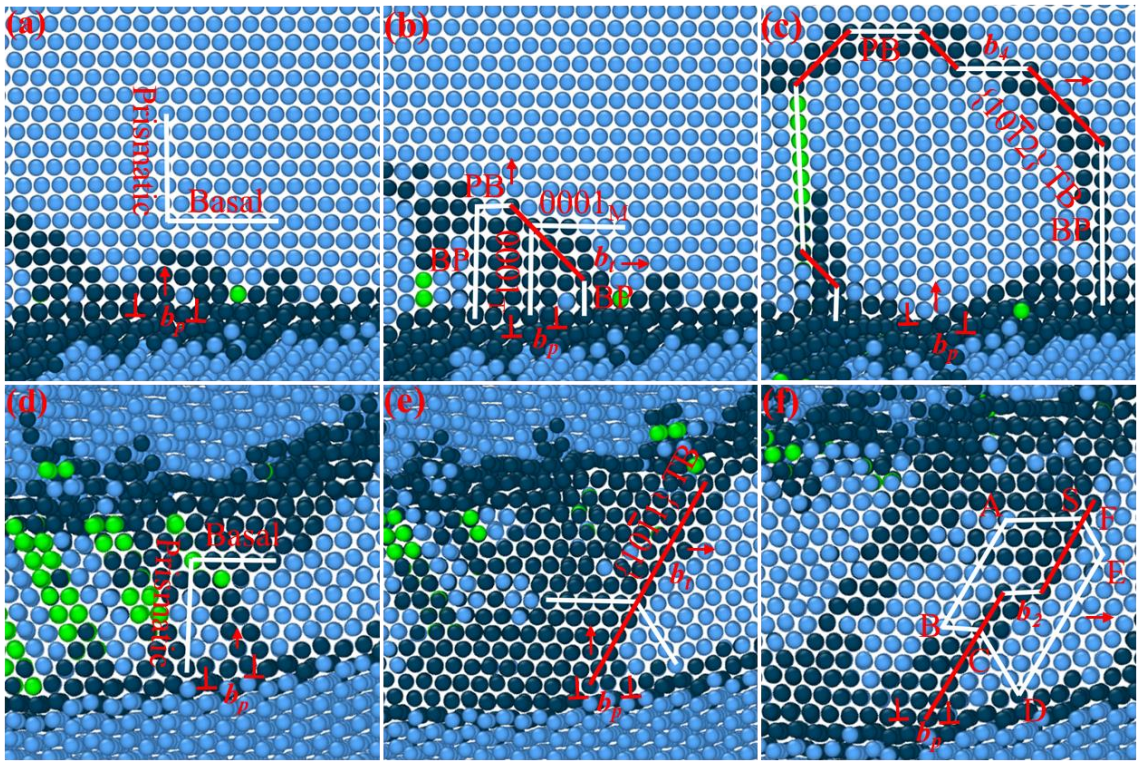

Fig. 9 Atomic structure evolutions show the nucleation and growth processes of TTW and CTW, respectively. (a)-(c) Nucleation and growth process of TTW. (d)-(e) Nucleation and growth process of CTW.

Atomic-scale snapshots for the nucleation and growth processes of TTW and CTW are shown in Fig. 9(a-c) and Fig. 9(d-f), respectively. As for the TTW case, basal <a> dislocations are first piled up in the GBs. Under an external applied shear stress from the SPDT process, basal <a> dislocations are dissociated into Shockley partials dislocation $\boldsymbol{b_p}$ in the basal plane, as indicated in Fig. 9(a), which will act as the heterogeneous nucleation sources for the TTW. As the external stress gradually increases with the SPDT pass, the small pile ups-induced local stress is increased to causes those atoms that are located at and/or in the vicinity of the core of partials dislocation $\boldsymbol{b_p}$ to shuffle into twinning nuclei, as shown in Fig. 9(b). Fig. 9(b) also shows that the TTW is surrounded by $\{10\bar{1}2\}$ coherent twin boundaries (CTBs) and several energetically favored PB/BP facets. In addition, a glissile TD ($\boldsymbol{b_t}$) should be left in the TB after

the decomposition of the lattice <a> dislocation. For the $\{10\bar{1}2\}$ TTW, $\boldsymbol{b}_t$ is determined as $\frac{3-\kappa^2}{3+\kappa^2}\langle\bar{1}011\rangle$. Note that the dislocation character of the TD is characterized by its Burgers vector, $\boldsymbol{b}$, and the associated steps in the cores of the TD with the step height, h. It was suggested that the value of h is dependent on the type of TD and usually consists of several crystallographic planes. Fig. 9(c) shows a four atomic-layer TD ($\boldsymbol{b}_4$) is indexed to be left on the TB of the grown $\{10\bar{1}2\}$ TTW. Therefore, the dislocation transmutation reaction for the formation of $\{10\bar{1}2\}$ TTW can be described as:

$$2\times\frac{1}{3}<\bar{1}\bar{1}20>_m\rightarrow \boldsymbol{b}_t+\frac{1}{3}<1\bar{2}1\bar{3}>_t \tag{6}$$

where the subscripts m and t denote the matrix and the twin, respectively. This $\boldsymbol{b}_4$ is also known as the twinning disconnection $\boldsymbol{b}_{-2/-2}$. It should be emphasized that the $<c+a>_t$ dislocation which results from this mechanism contains the <a> direction that is common to the matrix and twin. The growth of twin is realized by the migration of TBs, either by the gliding of TDs on the twin plane along the twinning direction or migration of TBs in the direction normal to the twin plane.

Compared with TTW, similar nucleation and growth process of CTW are observed in Fig. 9(d-f). However, some characteristics of CTW differ from that of the TTW. As for the CTW, firstly, the dislocation types piled up in the GBs are possibly either a basal or non-basal dislocation. Thus, the CTW are found in the depth layer that is closer to the topmost surface of the SPDT sample, where the higher stress for their nucleation can be provided. It has also been predicted that the critical resolved shear stress (CRSS) is 76~153 MPa of the $\{10\bar{1}1\}<10\bar{1}2>$ CTW, which is much higher than 2~3 MPa of $\{10\bar{1}2\}<10\bar{1}1>$ TTW in Mg alloys [36]. Secondly, Fig. 9(b-c) shows that the CTW is surrounded by CTB and steps with the heights ranging from one to several $(10\bar{1}1)$ atomic planes. Notably, these steps are the crucial traces to understand the TDs-dominated mechanism of the twin growth. As shown in Fig. 9(f), a two atomic-layer step ($\boldsymbol{b}_2$) is observed in the $\{10\bar{1}1\}$ TB of CTW. It was reported 2-layer TDs are more mobile than other type TDs [37]. Fig. 9(f) gives a closed circuit SABCDEF that is constructed around $\boldsymbol{b}_2$. The constituent elements of the circuit are along the $[1\bar{2}10]$ projection.

The $\boldsymbol{b_2}$ is equal to $\frac{4\kappa^2-9}{2(4\kappa^2+3)}[\bar{1}01\bar{2}]+\frac{1}{6}[\bar{1}2\bar{1}0]$. Combined with the HRTEM image as shown in Fig. 5(c), the large relative displacements along the TB are presented in the view along the $[1\bar{2}1\bar{3}]$ direction, as well as the $[1\bar{2}10]$ direction.

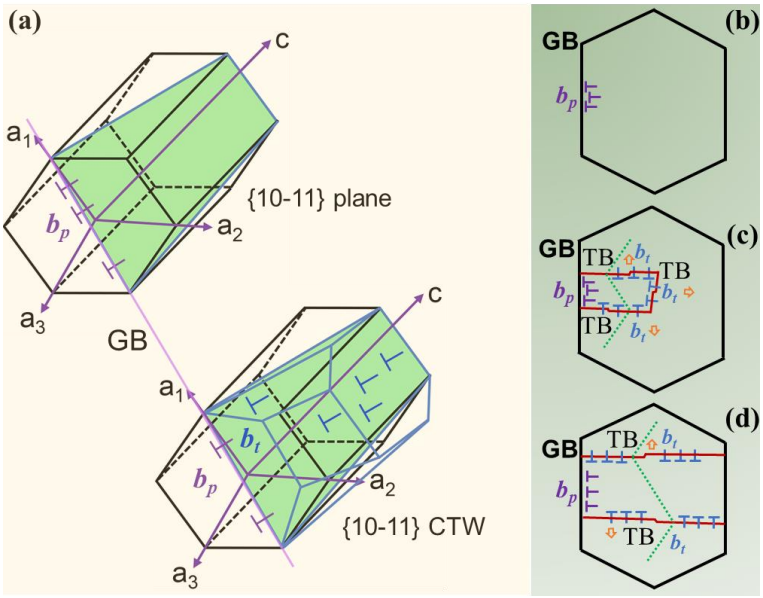

Fig. 10 Schematic of twinning nucleation and growth of (a) $\{10\bar{1}1\}$ CTW. Summary of twinning nucleation and growth in GNS L4 alloy based on HRTEM and MD results: (b) partial dislocations pile up at GBs, (c) nucleation of twinning, (d) growth of twinning.

Fig. 10(a) exhibits the 3D schematic illustration of $\{10\bar{1}1\}$ CTW. The crystallographic relation of the twin lattice is rotated around the $<\bar{1}2\bar{1}0>$ axis direction by 56.17 ° for the $\{10\bar{1}1\}$ twin. The axis of rotation corresponds to the normal direction of the plane of shear. Based on the microstructural evolution dissected by MD simulations and experimental HRTEM characterizations in our study, the nucleation and growth mechanisms of DTWs during the SPDT process are schematically summarized in Fig. 10(b)-(d). First, high density of dislocations pile up in the GBs in the L4 alloy during the SPDT process evidenced in TEM observations. GBs not only can act as heterogeneous nucleation sources of twinning, but also favor the high stress concentrations to overcome the reaction barriers for nucleation. Then, the partial dislocations are dissociated from dislocations at the GBs, i.e., either basal or non-basal dislocations for the nucleation of CTW, respectively. The growth of twinning is taken place by gliding of TDs along twin directions on twin planes. Under an applied shear stress, these defects provide a source of new glissile TDs. The glide of two TDs away from the defect moves the twin front but leaves the defect in the interface. There, it can continue to provide further TDs,

without the need for additional lattice dislocations.

5.2 Transition of deformation mechanisms during the GNS refinement process

The Hall-Petch relationship with effective stress (σ_y) against the square root of grain size ($d^{-1/2}$) along the gradient direction are plotted in Fig. 11(a) to elucidate the transition of deformation mechanisms during the GNS refinement process. Based on the XRD results, the GNS layer shows random orientations. Therefore, the effects of texture on the H-P relationship are ignored in our study. The effective stresses are estimated from the measured nanoindentation hardness H in Fig. 2(d) based on the Tabor relationship, i.e., $H = 3\sigma_y$ [38]. Fig. 11(a) clearly demonstrates two linear regions, i.e., linear low-stress (large-grain size) Hall-Petch region I and linear high-stress (small-grain size) Hall-Petch region II, implying a transition of deformation mechanisms in these two regions. Accordingly, Hall-Petch relationship expressed as: [39, 40]

$$\sigma_y = \sigma_0 + kd^{-1/2} \tag{7}$$

can be used to determine the values of material dependent constants σ_0 and k in these two linear regions. A physical basis for these material dependent constants is associated with the difficulty of dislocation movement across GBs and stress concentration due to dislocation pile-up. As a result, the linearly fitting gives a larger Hall-Petch slope $k = 151.8$ MPa$\sqrt{\mu m}$ in the low-stress region I (grain size ranging from 2.45 μm to 21 μm), while a smaller Hall-Petch slope $k = 24.6$ MPa$\sqrt{\mu m}$ in the high-stress region II (grain size ranging from to 70 nm to 2.45 μm), indicating the transition of deformation mechanisms a critical grain size of 2.45 μm. It is generally accepted that twinning-dominated plastic deformation gives a large Hall-Petch slope (e.g., the order of hundreds MPa$\sqrt{\mu m}$ or above), while dislocation-dominated plastic deformation possesses a small one (e.g., lower than 100 MPa$\sqrt{\mu m}$). In addition, Fig. 11(a) also gives the Hall-Petch plots for some other Mg alloys from the literatures, suggesting a similar transition of plastic deformation based on the approximately Hall-Petch slopes in the same linear region. For example, the plastic deformation of the extruded L4 alloy ($k = 238.8$ MPa$\sqrt{\mu m}$) [41] and LZ52 alloy ($k = 148.6$ MPa$\sqrt{\mu m}$) [42] in the region I with relatively

high Hall-Petch slopes in Fig. 11(a) have been suggested to be associated with the activation of TTWs. The mechanism of deformation twinning was also reported to be activated by performing *in-situ* TEM nanomechanical tests on pure Mg pillar with k = 306.3 MPa$\sqrt{\mu m}$ [43]. Notably, the dominated deformation mechanisms transiting from twinning to dislocation has also been reported in AZ31 alloys with the grain sizes transiting from 0.59-2.34 μm (k = 208.2 MPa$\sqrt{\mu m}$) in region I to 2.85-33 μm (k = 39.9 MPa$\sqrt{\mu m}$) in region II [44, 45], as shown in Fig. 11(a). Combining the observed microstructural evolution in this work, therefore, we confirm that the transition of dominated plastic deformation from twinning in FGs (grain sizes from 2.45 μm to 21 μm) to dislocation in UFGs and NGs (grain sizes from 2.45 μm to 70 nm) is occurred in the refinement process of the GNS layer on SPDT L4 alloy.

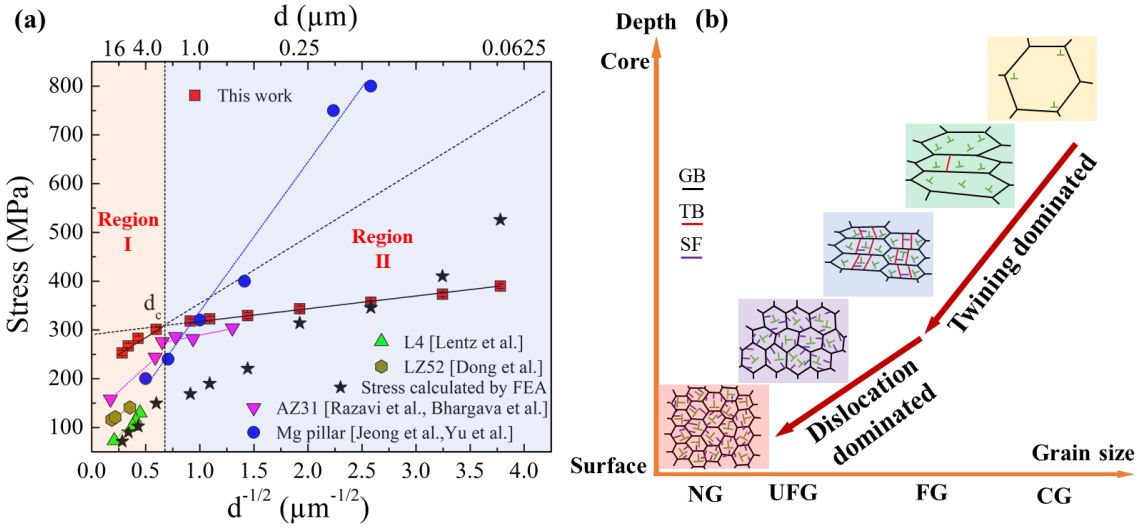

Fig. 11 (a) Effective stresses of various Mg alloys plotted against grain size showing Hall-Petch relationship and corresponding dominated plastic deformation mechanisms for the refinement process. (b) Schematic illustration of grain refinement process in L4 GNS layer from the matrix to surface.

Compared with the metals with cubic structures, the HCP structural Mg alloys have more complicated deformation modes, which may include basal <a> slip, prismatic <a> slip, pyramidal <c+a> slip, and deformation twinning with $\{10\bar{1}2\}$ TTW and $\{10\bar{1}1\}$ CTW. The activation of these deformation modes is related to their size-dependent CRSS and deformation compatibilities to coordinate the plastic deformation. Without component along the <c> direction, basal and prismatic <a> slips possess the lowest CRSS and they should be the preferred deformation modes in the early stage of plasticity, as the experimental observations in Fig. 3(a). Notably, only four independent slip systems can be provided by them together,

which make them difficult to meet the von-Mises criterion for the later arbitrary deformation. Therefore, either deformation twinning or pyramidal <c+a> slip become an alternative deformation mode for Mg alloys to accommodate the deformation along <c> direction.

Owing to its relatively low CRSS in normal CGs or FGs, deformation twinning has been theoretically and experimentally proven to be the dominant deformation mechanism to maintain the necessary deformation capability and coordinate the plastic deformation, as HRTEM observations and MD simulations in the present work. The level of CCRS can be analogous to the effective stress for the Hall-Petch plot in Fig. 11(a), in which the required stress for the dominant deformation twinning in region I (grain size from 2.45 μm to 21 μm) is obvious lower than that for pyramidal <c+a> dislocation slip. However, it becomes apparently higher than that for dislocation slip once the grain size decreasing to region II, leading to the transition of deformation mechanism. This is because the deformation twinning possesses a larger Hall-Petch slope k_{DT} relative to the k_{DS} for ordinary dislocation slip, i.e., $k_{DT} >> kDS$, which has also been widely reported in literature as mentioned above. In other words, it means that deformation twinning is more sensitive to the grain size, and thus GBs act as stronger resistance for deformation twinning than dislocation slip. To name a few, the critical stress for twinning nucleation in Mg-Ce alloy is higher than 1 GPa when the grain size is reduced to nanoscale [46]. It is also reported the average nucleation stress for the CTW under nanocompression is ~750 MPa and that for TTW in tension is ~800 MPa in the Mg alloys with the average grain size ~200 nm [47]. Note that the thickening of deformation twinning is by perfectly correlated layer-by-layer stimulating or promoting of twinning dislocations to penetrate adjacent parallel planes with the same Burgers vector. In this regard, a ‘‘stimulated slip’’ model for deformation twinning in HCP materials has been proposed [48] after comparing with the Tayler model, i.e., $k_{DT} = \kappa Eb(P_{promoter})^{-1/2}$, in which E is the Young's modulus, b is the Burgers vector, κ is a dimensionless constant of order 1, and P_{promoter} ($0< P_{\text{promoter}} <1$) is the fraction of the total dislocation population act as "promoter" twinning dislocations. Since the GB surface in polycrystalline materials will determine the confined volume to restrict the number of dislocations and dislocation activities, it has been commonly accepted that the number of available ‘‘promoters’’ is significantly reduced in finer grains with smaller volumes.

Therefore, the formation of deformation twinning in our L4 alloys becomes harder and harder during the further grain refinement process. On the other hand, the pre-formed deformation twinning in FGs, which reorients the HCP Mg lattice to "hard" crystallographic orientation, is equivalent to the reduction of the grain size and it would introduce extra barriers to "promoter" twinning dislocations. It is also therefore more and more difficult to form the high-order twins insides of twin fragments, especially whose size down to nanoscale in the further refinement as the SPDT process continues.

Conversely, the situation for pyramidal <c+a> slip differs greatly from the deformation twinning. The CRSS for non-basal pyramidal <c+a> slip is normally ~100 times of the basal slip, i.e., CRSS anisotropy of $\tau_{CRSS}^{nonbasal} / \tau_{CRSS}^{basal} \approx 100$. However, when the strength of HCP alloys is close to the ideal strength and saturated in finer grains, the high strengths and shorter dislocation lengths can help to turn on alternative dislocation slip behavior. For example, it has been reported that the anisotropy CRSS between pyramidal <c+a> slip and basal <a> slip is reduced from ~100 to ~2 when the grain size refined from microns to nanometers [49]. As a result, pyramidal <c+a> slip system instead of twinning plays a critical role in the grain refinement process in finer grains. More specifically, with the increase of the strain/strain rate during the further refinement process, the dense dislocation arrays in subgrains, including basal, prismatic and pyramidal dislocations, would cooperatively induce lattice/grain rotation DRX, as analyzed from Fig. 6. Different dislocation slip systems will cause different rotation direction, which would increase the misorientation between subgrains and eventually results in the high angle GBs for the formation of the NGs in the top surface layer.

The equivalent stress of the surface estimated by FEA is also plotted in Fig. 11 (a). The equivalent stress of surface is apparently lower than the critical equivalent stress for deformation twinning, but higher than that for dislocation slip. Therefore, it leads to the dislocation slip-dominated deformation mechanism in the topmost surface layer with grain size of ~ 70 nm in the SPDT L4 alloy, agreement with the results of HRTEM analysis and MD simulations. Fig. 11(b) schematically summarizes the grain refinement process in the L4 GNS layer from the matrix to surface during the SPDT process. At the early stage of the SPDT process, the plastic deformation is governed by basal dislocation slip and few TTWs, which

divides the original CGs into lamellar FGs. With increasing strain rate and stress exerted in the SPDTed sample, TTWs and CTWs successively prosper within the lamellar FGs. Then deformation twinning processes are saturated with the decreasing grain size. Then nonbasal-mediated dislocation slips become the main deformation mechanism again for the further deformation for UFGs. Finally, NGs are refined by dislocation slips-induced rotation DRX. Note that pure Mg has low melting point (650 °C), the melting point of L4 alloy is lower than that of pure Mg from the theoretical point of view. A low melting point corresponds to a low DRX temperature. Moreover, the DRX even can occur at room temperature when the strain and strain rate are quite high in Mg alloys [50]. During the SPDT process, the strain rate at the topmost surface could reach up to 10^3~10^5 s^{-1}, which have been proven to lead to the effective grain refinement by DRX process [20]. In addition, the non-basal slips correlated SFs facilitate the formation of low-angle grain boundaries that can subsequently transition into high-angle grain boundaries. As a result, a high density of defects inside the substructures appears and NGs are formed after rotation recrystallization process at room temperature.

6 Concluding Remarks

In this work, a novel facile high-speed machining method named SPDT has been developed to produce effectively the GNS layer on HCP Mg alloy. The grain refinement process and underlying plastic deformation mechanisms of the GNS layer are dissected at the atomic level mainly by HRTEM characterizations, atomistic MD simulations as well as FEA. The major findings are summarized as follows:

(1) A GNS layer with thickness of about 65 μm is achieved on Mg-4Li alloy processed by SPDT. The grain refinement process of this GNS layer consists of elongated CGs, FGs with TTWs and CTWs, UFGs and NGs along the depth direction from inner matrix to topmost surface. The average size of NGs in the topmost surface is about 70 nm.

(2) Two types of deformation twins are nucleated by partial dislocations decomposed from the lattice dislocation pile up at GBs. More specifically, partial dislocations for the TTW are decomposed from basal <a> dislocations. While either basal dislocations or non-basal dislocations are converted to partial dislocations for the CTW, which requires higher local stress concentrations in the depth layer that is closer to the topmost surface. The growth of the

twins is attributed to the TDs gliding on the twinning plane along the twinning direction.

(3) The underlying plastic deformation mechanisms for the grain refinement process of the GNS layer are grain size-dependent. The plastic deformation mechanisms of basal dislocation slip, TTW, DTW, and non-basal dislocation slip are successively activated to refine the grains along the gradient direction from inner core to surface with gradually increasing exerted stress. The rotation DRX induced by dislocations are responsible for the refinement of the NGs. Particularly, a critical grain size of 2.45 μm is determined for the dominated deformation mechanism transiting from deformation twinning in FGs to dislocation slip in UFGs and NGs. Moreover, the Hall-Petch relationship plot along the gradient direction and the surface equivalent stress calculated by FEA for the SPDT process are incorporated to quantitatively elucidate the transition in the deformation mechanisms.

Declaration of competing Interest

The authors declare no competing financial interests.

Acknowledgements

The authors acknowledge the support from the National Natural Science Foundation of China Projects (Nos. 51701171 and 51971187) and the support by the funding support to Partner State Key Laboratories in Hong Kong from the Innovation and Technology Commission (ITC) of the Government of the Hong Kong Special Administration Region (HKASR), China. The authors would also like to express their sincere thanks to the financial support from the PolyU Research Office (Project Code: 1-BBXA).

References

1. E. Ma, T. Zhu, Mater. Today 20 (2017) 323-331.
2. K. Lu, Science 345 (2014) 1455-1456.
3. X. Wu, P. Jiang, L. Chen, F. Yuan, Y.T. Zhu, P. Natl. Acad. Sci. USA 111 (2014) 7197-7201.
4. Z. Cheng, H. Zhou, Q. Lu, H. Gao, L. Lu, Science 362 (2018)
5. X. Chen, Z. Han, X. Li, K. Lu, Sci. Adv. 2 (2016) e1601942.
6. X. Zhou, X.Y. Li, K. Lu, Science 360 (2018) 526.
7. J.Y. Kang, J.G. Kim, H.W. Park, H.S. Kim, Sci. Rep. 6 (2016) 26590.
8. M.N. Hasan, Y.F. Liu, X.H. An, J. Gu, M. Song, Y. Cao, Y.S. Li, Y.T. Zhu, X.Z. Liao, Int. J. Plasticity 123 (2019) 178-195.

9. J.Z. Lu, K.Y. Luo, Y.K. Zhang, C.Y. Cui, G.F. Sun, J.Z. Zhou, L. Zhang, J. You, K.M. Chen, J.W. Zhong, Acta Mater. 58 (2010) 3984-3994.
10. W. Guo, Z. Pei, X. Sang, J.D. Poplawsky, S. Bruschi, J. Qu, D. Raabe, H. Bei, Acta Mater. 170 (2019) 176-186.
11. W.S. Miller, L. Zhuang, J. Bottema, A.J. Wittebrood, P. De Smet, A. Haszler, A. Vieregge, Mat. Sci. Eng. A 280 (2000) 37-49.
12. Z. Zurecki, R. Ghosh, J.H. Frey. *ASME 2003 International Mechanical Engineering Congress and Exposition*. 2003.
13. J.J. Wang, N.R. Tao, K. Lu, Acta Mater. 180 (2019) 231-242.
14. J. Azadmanjiri, C.C. Berndt, A. Kapoor, C. Wen, Crit. Rev. Solid State 40 (2015) 164-181.
15. Y. Wei, Y. Li, L. Zhu, Y. Liu, X. Lei, G. Wang, Y. Wu, Z. Mi, J. Liu, H. Wang, and H. Gao, Nat. Commun. 5 (2014) 3580.
16. A.Y. Chen, H.H. Ruan, J. Wang, H.L. Chan, Q. Wang, Q. Li, J. Lu, Acta Mate. 59 (2011) 3697-3709.
17. X.-S. Yang, S. Sun, T.-Y. Zhang, Acta Mater. 95 (2015) 264-273.
18. X.-S. Yang, S. Sun, H.-H. Ruan, S.-Q. Shi, T.-Y. Zhang, Acta Mater. 136 (2017) 347-354.
19. M. Yoo, Metall. Trans. A 12 (1981) 409-418.
20. H.Q. Sun, Y.N. Shi, M.X. Zhang, K. Lu, Acta Mater. 55 (2007) 975-982.
21. X.Y. Shi, Y. Liu, D.J. Li, B. Chen, X.Q. Zeng, J. Lu, W.J. Ding, Mat. Sci. Eng. A 630 (2015) 146-154.
22. L. Chen, F. Yuan, P. Jiang, J. Xie, X. Wu, Mat. Sci. Eng. A 694 (2017) 98-109.
23. S. Suet To, V.H. Wang, W.B. Lee, *Single Point Diamond Turning Technology*, 2018, Springer Berlin Heidelberg: Berlin, Heidelberg.
24. T. Al-Samman, Acta Mater. 57 (2009) 2229-2242.
25. Y.-M. Kim, I.-H. Jung, B.-J. Lee, Model. Simul. Mater. Sci. 20 (2012) 035005.
26. G.R. Johnson, W.H. Cook, Eng. Fract. Mech. 21 (1985) 31-48.
27. Z. Pu, D. Umbrello, O.W. Dillon, T. Lu, D.A. Puleo, I.S. Jawahir, J. Manuf. Process. 16 (2014) 335-343.
28. X. Wang, L. Jiang, C. Cooper, K. Yu, D. Zhang, T.J. Rupert, S. Mahajan, I.J. Beyerlein, E.J. Lavernia, J.M. Schoenung, Acta Mater. 195 (2020) 468-481.
29. F. Wang, S.R. Agnew, Int. J. Plasticity 81 (2016) 63-86.
30. S.Q. Zhu, S.P. Ringer, Acta Mater. 144 (2018) 365-375.
31. J. Tang, H. Fan, D. Wei, W. Jiang, Q. Wang, X. Tian, X. Zhang, Int. J. Plasticity 126 (2020) 102613.
32. R.C. Pond, D.J. Bacon, A. Serra, Phil. Mag. Lett. 71 (1995) 275-284.
33. Q. Zu, X.-Z. Tang, H. Fu, Q.-M. Peng, Y.-F. Guo, Mater. 5 (2019)
34. M. Efe, W. Moscoso, K.P. Trumble, W. Dale Compton, S. Chandrasekar, Acta Mater. 60 (2012) 2031-2042.
35. Y. Guo, C. Saldana, W. Dale Compton, S. Chandrasekar, Acta Mater. 59 (2011) 4538-4547.
36. J. Koike, Mater. Trans. A 36 (2005) 1689–1696.
37. J. Wang, I.J. Beyerlein, J.P. Hirth, C.N. Tomé, Acta Mater. 59 (2011) 3990-4001.
38. D. Tabor, *The hardness of metals*. 2000: Oxford university press.
39. E.O. Hall, Proc. Phys. Soc. Sect. B 64 (1951) 747.
40. N. Petch, J. Iron Steel Inst. 174 (1953) 25-28.
41. M. Lentz, M. Klaus, I.J. Beyerlein, M. Zecevic, W. Reimers, M. Knezevic, Acta Mater. 86 (2015) 254-268.
42. H. Dong, F. Pan, B. Jiang, Y. Zeng, Mater. Design 57 (2014) 121-127.

43. J. Jeong, M. Alfreider, R. Konetschnik, D. Kiener, S.H. Oh, Acta Mater. 158 (2018) 407-421.
44. S.M. Razavi, D.C. Foley, I. Karaman, K.T. Hartwig, O. Duygulu, L.J. Kecskes, S.N. Mathaudhu, V.H. Hammond, Scripta Mater. 67 (2012) 439-442.
45. G. Bhargava, W. Yuan, S.S. Webb, R.S. Mishra, Metall. Mater.Trans.s A 41 (2009) 13-17.
46. J. Ye, R.K. Mishra, A.K. Sachdev, A.M. Minor, Scripta Mater. 64 (2011) 292-295.
47. Q. Yu, L. Qi, K. Chen, R.K. Mishra, J. Li, A.M. Minor, Nano Lett. 12 (2012) 887-92.
48. Q. Yu, Z.W. Shan, J. Li, X. Huang, L. Xiao, J. Sun, E. Ma, Nature 463 (2010) 335-8.
49. Q. Yu, L. Qi, R.K. Mishra, J. Li, A.M. Minor, P. Natl. Acad. Sci. USA 110 (2013) 13289-13293.
50. K. Xu, A. Wang, Y. Wang, X. Dong, X. Zhang, Z. Huang, Appl. Surf. Sci. 256 (2009) 619-626.